Nonspherical and spherical characterization of ice in Hurricane Erin for wideband passive microwave comparisons

Gail Skofronick-Jackson,[1] Andrew Heymsfield,[2] Eric Holthaus,[3] Cerese Albers,[4] and Min-Jeong Kim[5]

Received 20 April 2007; revised 20 September 2007; accepted 5 December 2007; published 18 March 2008.

[1] In order to better understand the characteristics and physical-to-radiative relationships of frozen hydrometeors in hurricane systems, computed brightness temperatures (T_B) from 10.7 to 183 ± 10 GHz were compared with radiometric observations of Hurricane Erin (2001) from the NASA ER-2 aircraft. The focus was on the high frequencies (≥85 GHz) that are particularly sensitive to frozen hydrometeors. In order to initialize the cloud profiles used in the radiative transfer calculations, data from airborne radars, dropsondes, and cloud models were used. Three different ice habit and size parameterizations were used with these cloud profiles to obtain the particle radiative signatures including (1) spherical particles with size distributions derived from in situ observations, (2) spherical "fluffy" snow and graupel particles with modified Marshall-Palmer size distributions, and (3) a non-spherical bullet rosette habit where the radiation attributes (scattering, absorption, and asymmetry properties) were computed using the Discrete Dipole Approximation. In addition, three different reflectivity to ice water content (Z-IWC) relationships were used with the three habit and size parameterizations to provide a measure of the sensitivity of the Z-IWC relationship. This work showed that both the scattering and asymmetry coefficients, along with the ice water content in each layer, play an important role in determining the resultant high frequency brightness temperatures. All low frequency (<40 GHz) calculations matched the observations with correlation coefficients greater than 0.9. At higher frequencies (> 90 GHz), correlation coefficients ranged from 0.7 to 0.92. Comparing between the three ice habit and size parameterizations showed less than a 0.2 difference in correlation coefficient, while the comparisons between the three Z-IWC relationships caused changes of up to 0.15 in the correlation coefficients, but they had a significant effect on the mean differences between the observations and the calculations.

Citation: Skofronick-Jackson, G., A. Heymsfield, E. Holthaus, C. Albers, and M.-J. Kim (2008), Nonspherical and spherical characterization of ice in Hurricane Erin for wideband passive microwave comparisons, *J. Geophys. Res.*, *113*, D06201, doi:10.1029/2007JD008866.

1. Introduction

[2] The development and strength of tropical cyclones is highly influenced by frozen hydrometeors in hurricane rainbands and convection [e.g., *McFarquhar et al.*, 2006; *Heymsfield et al.*, 2006; *Willoughby*, 1998]. In fact "hot towers" associated with increasing hurricane intensity contain a significant amount of frozen hydrometeors. They are called hot towers because their column of air is slightly warmer than the surrounding air temperature, but above the melting layer at about 4–6 km to the tops of the towers at 15–19 km, the cloud hydrometeors are frozen. However, little information is known about frozen hydrometeor characteristics in hurricane and other clouds. While cloud resolving models do incorporate frozen hydrometeors [e.g., *Wu et al.*, 2006; *Tao et al.*, 2007], in general these modeled particles are only validated with extremely sparse in situ measurements or through comparisons between forward radiative transfer calculations using the model data and radiometer observations at frequencies up to 85 GHz. Unfortunately, the brightness temperature sensitivity to ice hydrometeors in clouds is limited by the physical and dielectric characteristics of ice for frequencies below 85 GHz. The sensitivity of higher frequency channels (~>85 GHz) to frozen hydrometeors has been proven [e.g., *Skofronick-Jackson et al.*, 2004; *Bennartz and Bauer*, 2003]. With these higher frequencies the relationships between wide-band radiometer observations and the physical and electromagnetic properties of frozen hydrometeors can be studied. Understanding these physical-radiative rela-

[1]NASA Goddard Space Flight Center, Greenbelt, Maryland, USA.
[2]National Center for Atmospheric Research, Boulder, Colorado, USA.
[3]Columbia University, New York City, New York, USA.
[4]Florida State University, Tallahassee, Florida, USA.
[5]NOAA, Camp Springs, Maryland, USA.

Copyright 2008 by the American Geophysical Union.
0148-0227/08/2007JD008866

tionships is important for developing algorithms in preparation for the Global Precipitation Measurement (GPM) mission launch in 2013 and for the retrieval of ice characteristics both above the melting layer, as in Hurricane Erin, and for frozen hydrometeors that reach the surface as falling snow.

[3] The microphysical characteristics and high frequency radiative properties of frozen hydrometeors are complex and difficult to ascertain without detailed in situ data sets. In and above the melting layer frozen hydrometeors can range from spherical to nonspherical habits and with varying mixtures of ice, air, and water in each particle. The methodologies for determining the single particle and bulk layer radiative properties of frozen hydrometeors rely on several assumptions and require computationally intensive numerical models. In the past, many investigators assumed spherical particles in order to reduce modeling complexities. More recently, the radiative properties for non-spherical frozen hydrometeors are being determined using the discrete dipole approximation [e.g., *Draine and Flatau*, 1994; *Liu*, 2004; *Kim*, 2006] and other models [e.g., *Xu and Gustafson*, 2001].

[4] The Fourth Convection and Moisture Experiment (CAMEX-4) provides a valuable database of active, passive, and in situ observations that is used to investigate the relationships between frozen hydrometeors and their radiative signatures. The CAMEX-4 field campaign was based in Jacksonville, Florida during August and September of 2001 [*Kakar et al.*, 2006]. This field campaign was a joint NASA and NOAA Hurricane Research Division project with the goal of studying tropical hurricane development, tracking, intensification, and land falling impacts. While remote sensing of the hurricane environment was the primary objective of CAMEX-4, there were also separate flights to study thunderstorm structure, precipitation systems, and atmospheric water vapor profiles. Multiple instruments located on ground, on low and high altitude aircraft, and on satellites were used to observe convective and hurricane systems. Of particular interest for this work are measurements from instruments on the high-altitude ER-2 aircraft at a ~20 km altitude that provide a single active radar channel and 19 passive microwave brightness temperature channels ranging from 10.7 to 183.31 ± 10 GHz during Hurricane Erin on 10 September 2001. The higher frequency channels are extremely useful for determining and constraining the particle size distributions of the frozen hydrometeors [*Skofronick-Jackson et al.*, 2003].

[5] The purpose of this research is to compare observed brightness temperatures to calculated brightness temperatures for several spherical and non-spherical frozen cloud hydrometeor habits in order to study how the selected ice shape and size parameterizations affect the radiative properties and resultant brightness temperatures. A radiative transfer model is employed to convert the hydrometeor parameterizations into brightness temperature values. The cloud profiles will be initialized with radar data through a conversion from reflectivity to hydrometeor content values and the sensitivity to these conversion relationships will be discussed. Other initialization procedures include determining boundary conditions and profile environmental conditions (e.g., surface wind speed and temperature, pressure, and relative humidity profiles) using dropsondes from the ER-2 and modeled Hurricane Erin data. The hydrometeor parameterizations (habits and particle size distributions for the frozen hydrometeors) are used to compute radiative properties (absorption, scattering, and asymmetry) that are required for use in radiative transfer calculations. Then the effects of these parameterizations on the computed brightness temperatures (T_B) are compared to the observed T_B.

[6] In section 2, details of the instruments and how the observations were co-located will be provided. The generation of the cloud hydrometeor profiles and initialization of boundary conditions will be described in section 3. In section 4 the habit and size distributions for the three parameterizations are provided, while in section 5 the radiative transfer model used in the brightness temperature calculations is summarized along with the radiative properties for each of the parameterizations. The comparisons between computed and observed brightness temperatures are analyzed in section 6, followed by a summary and discussion of the key points in section 7.

2. Observations

[7] While CAMEX-4 had broad-based instrumentation on multiple platforms including several aircraft and ground locations, this work focuses on the observations from four instruments on the ER-2 aircraft. On board the ER-2, flying at an altitude of approximately 20 km, the instruments of interest for this work are the High Altitude Monolithic Microwave Integrated Circuit (MMIC) Scanning Radiometer (HAMSR) [*Lambrigtsen and Riley*, 2002], the Advanced Microwave Precipitation Radiometer (AMPR) [*Spencer et al.*, 1994], the ER-2 Doppler Radar (EDOP) [*Heymsfield et al.*, 1996], and the ER-2 dropsonde system [*Halverson et al.*, 2006]. The first three instruments measure atmospheric hydrometeors in the microwave region of the electromagnetic spectrum, while the dropsondes are released from the ER-2 and measure temperature, relative humidity and wind speed in situ as they fall toward the Earth's surface. The HAMSR has 8 observations between 50 and 57 GHz, plus 166, 183.3 ± 1, 183.3 ± 1.8, 183.3 ± 3, 183.3 ± 4.5, 183.3 ± 7, and 183.3 ± 10 GHz, while the AMPR observes at the lower frequencies of 10.7, 19.35, 37, and 85.5 GHz. The EDOP is an active radar sampling at 9.6 GHz with a vertical range gate interval of 37.5 m and a minimum detectable level of ~−20 dBZ for this field campaign. HAMSR, AMPR, and EDOP are cross-track scanning instruments.

[8] The focus is on the rainbands and anvil regions associated with Hurricane Erin on 10 September 2001. As with many Atlantic tropical cyclones, Hurricane Erin can be traced back to a tropical wave from western Africa starting 30 August 2001. Erin continued to strengthen and became a hurricane by 0000 UTC 9 September, reaching its peak intensity near 0000 UTC 10 September. On 10 September, the vertical wind shear peaked and Erin began moving over cooler waters. In response, Erin began to weaken. By 0000 UTC 15 September, Erin had turned into a tropical storm and eventually transitioned into an extratropical system. The GOES satellite image of Hurricane Erin on 10 September 2001 is provided in Figure 1 with the ER-2 aircraft flight line superimposed on top of it. The portion of the ER-2 flight line investigated in this work is identified by a thick white line in Figure 1. The flight line begins at 33.9 N,

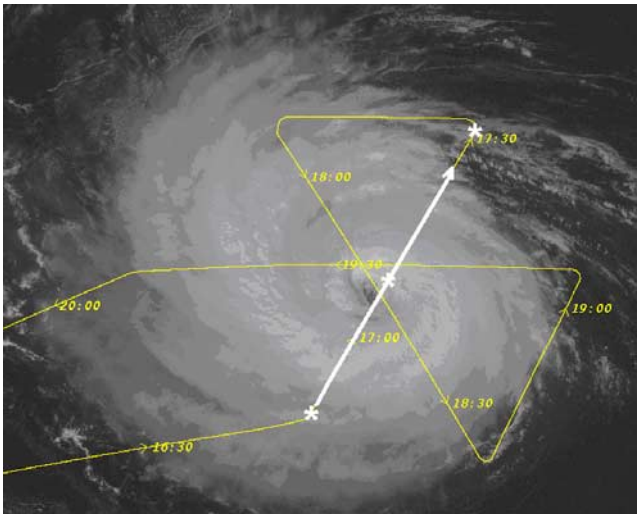

Figure 1. Visible GOES image with 10 September 2001 ER-2 aircraft flight track superimposed. The flight line of interest in this work is identified with a thick white line with an arrow showing flight direction. Stars indicate three dropsonde release locations.

66.14 W and goes to 37.22 N, 63.64 W in a straight line and extends over about 450 km. Only the nadir or near-nadir signatures are used in this analysis. Figure 1 also indicates the location of dropsonde releases from the ER-2 aircraft. These were the first successful dropsonde releases from a high altitude aircraft in a hurricane [*Halverson et al.*, 2006].

[9] The CAMEX-4 instrument set did include the capability to measure habits and particle size distributions (PSDs) in situ. Such instruments were flown on the DC-8 aircraft with a maximum altitude of ~12 km. The in situ particle sampling instruments only obtain PSDs at the altitude of the DC-8 aircraft and spirals of the aircraft are required to get PSDs over the vertical space of the cloud. While CAMEX-4 had a few coordinated ER-2 overpasses of the DC-8 spiraling through convective clouds, unfortunately this did not occur on the 10 September 2001 flights for Hurricane Erin.

[10] Figure 2 shows the EDOP, HAMSR, and AMPR observed data for Hurricane Erin on 10 September 2001 between 16:49:59 UTC and 17:25:00 UTC, including EDOP data (Figure 2a), selected HAMSR brightness temperatures (Figures 2b and 2c), and AMPR brightness temperatures (Figure 2d). This data was collected from the CAMEX-4 website. For this image, the ER-2 is flying toward the northeast as indicated in Figure 1. In the image the hurricane eye is surrounded by several rainbands with anvil, convective, and stratiform regions. From Figure 2c, it can be discerned that the higher frequencies of the HAMSR data (≥166 GHz) are sensitive to the frozen hydrometeors in the cloud (as indicated by non-zero reflectivities above the melting layer in the EDOP image collocated with depressions in the brightness temperatures at 166 and 183 GHz). On the other hand, the AMPR lower frequency channels (Figure 2d) are sensitive to the liquid in the rainbands. In fact, if the reflectivities of Figure 2a are summed from 0 to 4 km (the liquid part of the cloud) they have a correlation coefficient of 0.61, −0.20, and −0.28 with respect to 10, 85 and 183 ± 7 GHz, respectively. So 10 GHz is positively correlated with low altitude reflectivities, i.e., 10 GHz warms when the summed reflectivity values are higher. On the other hand, reflectivities summed from 5 km to the top of the cloud (frozen part of the cloud) generate correlation coefficients of 0.36, −0.52, and −0.64 for 10, 85 and 183 ± 7 GHz, respectively, meaning that 85 and 183 brightness temperatures decrease when the high altitude reflectivities increase. Although not readily apparent in Figure 2b, the 50 to 60 GHz band of the HAMSR instrument is typically used for temperature profiling with the lower frequencies sensing more about the lower altitudes and vice versa for the slightly higher frequencies.

[11] The data sets from the AMPR, HAMSR, and EDOP have been analyzed and collocated. The largest footprint of 2.8 km occurs for the AMPR 10 and 19 GHz channels at nadir when the ER-2 is flying at 20 km altitude. Because there is not an AMPR pixel directly at nadir, the two pixels adjacent to nadir were averaged to simulate a nadir value. The HAMSR footprint resolution is about 2.0 km at nadir. However, the HAMSR data samples were separated by about 12 s, therefore the footprint centers were separated by about 2.5 km based on a 205 m s^{-1} aircraft speed. Since the HAMSR and AMPR footprint resolutions and locations are so similar, the collocation process was simplified. Thus AMPR, HAMSR, and closest EDOP times were matched to the 183 points in the HAMSR data over this flight time.

3. Cloud Profile Initialization

[12] Prior to computing brightness temperatures for these 183 observational data points, a cloud profile data set must first be generated. The radar reflectivity can provide some information about the hydrometeors, however additional data about the atmospheric profile and boundary conditions are required. There are three steps: (1) the EDOP radar reflectivities are converted into vertical hydrometeor content profiles, (2) the temperature, pressure, and relative humidity profiles need to be determined, and (3) the boundary conditions for the ocean surface and top of atmosphere must be assigned. In order to obtain the required information for steps 2 and 3, dropsonde and hurricane model data is used. The role of the dropsondes is to provide detailed information about the temperature and relative humidity profiles that is not adequately generated by the simulated Hurricane Erin.

3.1. Hydrometeor Content Profiles

[13] Nadir-viewed EDOP radar reflectivity profiles are first corrected for attenuation using the technique of *Hitschfeld and Bordan* [1954] and then converted into estimates of hydrometeor content profiles. The fine (37.5 m) resolution of the radar range gates from 0 to ~18 km is averaged to 0.25 km vertical slabs. The hydrometeor content profiles from the radar-to-microphysical profile algorithm are partitioned into liquid and frozen hydrometeors with exponential drop size distributions, respectively. While continuity of the precipitation flux across the freezing level is not explicitly enforced, the masses obtained from the radar reflectivities have smooth transitions from one level to the next.

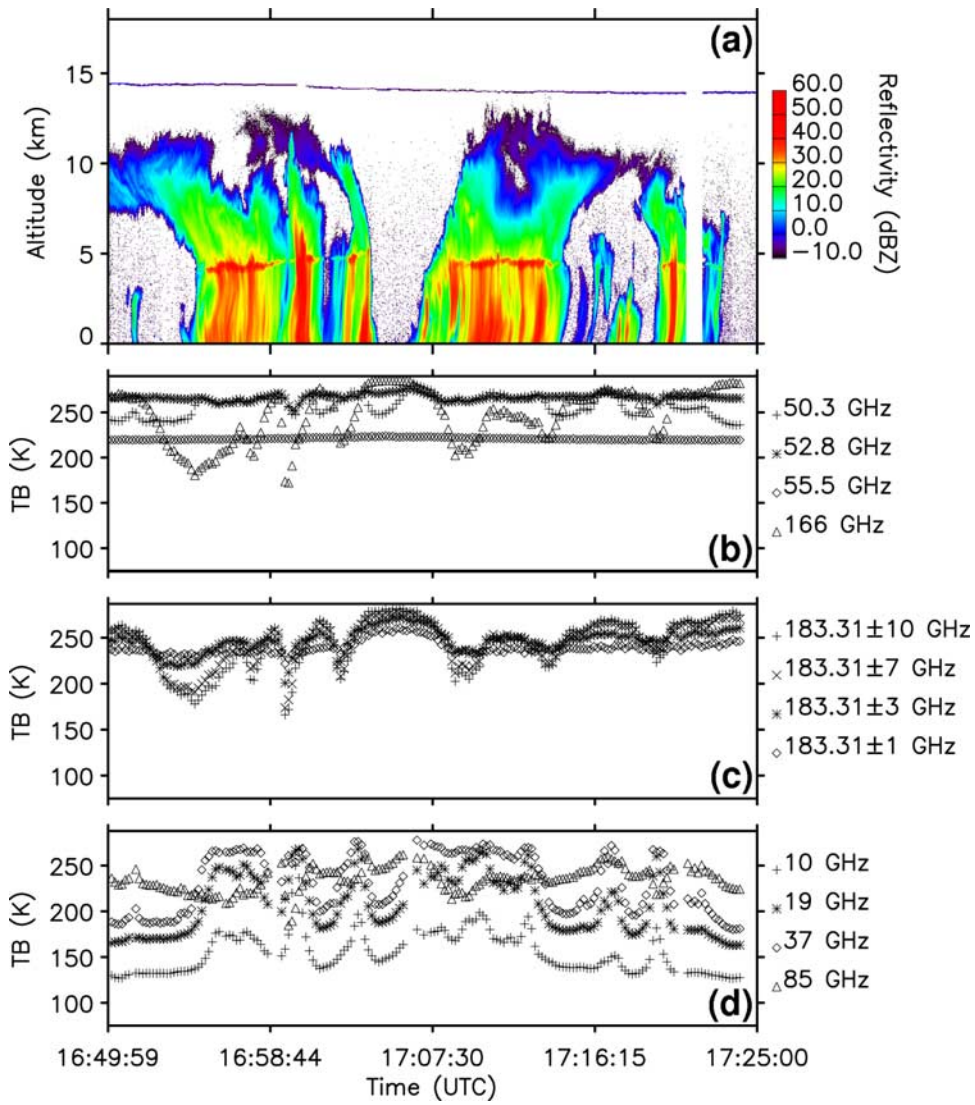

Figure 2. Collocated EDOP-HAMSR-AMPR Hurricane Erin data set from 10 September 2001.

[14] The averaged reflectivities are converted to rainwater content using the *Marshall and Palmer* [1948] relationship:

$$M_L(m,h) = 0.0055(Z_{obs}(m,h))^{0.55}\,\mathrm{g\,m^{-3}} \quad (1)$$

where M_L is the mass content of the liquid particles at the flight pixel m and height level h associated with the attenuated corrected EDOP reflectivity Z_{obs} (in $\mathrm{mm^6\ m^{-3}}$). Once the temperature in the vertical profile reaches 0°C a portion of the content derived from Z_{obs} is reserved for frozen hydrometeors. A linear interpolation is used to transition to all frozen hydrometeors at −22.5°C and colder such that both liquid and frozen hydrometeors exist between 0 and −22.5°C. While there are more detailed procedures for modeling the melting layer [*Olson et al.*, 2001], the linear method used in this work does not detract from the overall results of this paper since it is applied consistently for all cases. Because of the complexities and unknowns of melting layer ice particle characteristics and their radiative properties, no physically melting particles were included in this analysis. However, the findings of *Skofronick-Jackson et al.* [2002] can be used to predict the change in T_B if a melting layer were added. The conversion from reflectivity to frozen hydrometeor content at each level is defined by the commonly used power law relationship between attenuation-corrected reflectivity observations Z_{obs} and ice water content, IWC, (also denoted as M_F) as follows:

$$M_F(m,h) = a[Z_{obs}(m,h)]^b\,\mathrm{g\,m^{-3}}. \quad (2)$$

As a baseline in this work, $a = 0.103$ and $b = 0.33$ are derived from in situ observations of IWC along with reflectivity measurements at X-band (same as EDOP) during the Cirrus Regional Study of Tropical Anvils and Cirrus Layers-Florida Area Cirrus Experiment (CRYSTAL-FACE) field campaign [*Jensen et al.*, 2004]. Figure 3 shows the fitted data set for this Ze-IWC relationship. While the CRYSTAL-FACE observations are from anvils and convective outflow regions, and not hurricanes, they provide relationships in a temperature range from approximately 0 to −60°C and for

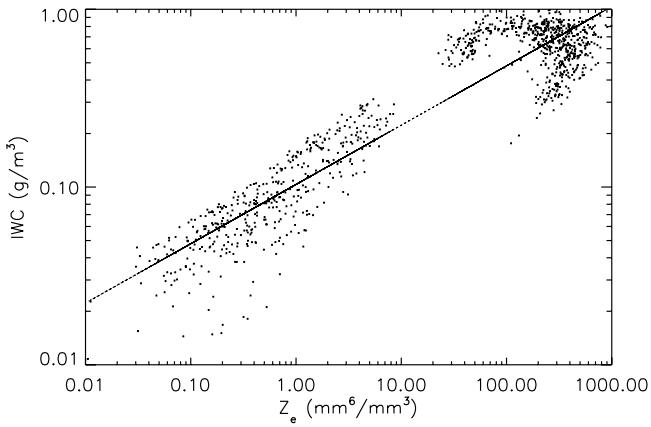

Figure 3. CRYSTAL-FACE reflectivity versus IWC and curve fit of IWC = 0.103 $Ze^{-0.33}$.

reflectivities ranging from −20 dBZ to 30 dBZ [*Heymsfield et al.*, 2007]. Further, while it is likely that the Z-IWC relationships (and particle size distributions) will vary over the different regions of the storm, no adjustments were made for convective versus stratiform regions because of the difficulty in consistently and robustly classifying such systems. Section 6 will have a discussion on the sensitivity of the brightness temperature calculations to the assumed Z-IWC relationship(s).

[15] EDOP radar reflectivities cannot provide information on cloud water and cloud ice contents because it is not sensitive enough. Further, the modeled data is not trustworthy with respect to the implementation and resulting cloud water and cloud ice fields. Thus cloud water and cloud ice fields are not explicitly included as cloud particles. However, the size distributions of the rain and ice allow for particles as small as cloud water and cloud ice. Also, it has been known that supercooled cloud water exists only in the strongest hurricane updrafts [*Willoughby et al.*, 1985; *Black and Hallett*, 1986]. Since there are only a few locations of updraft in the observed data, for simplicity, supercooled water was not added to the profiles in these regions. The transformation from reflectivities to particle contents described above populates the liquid and frozen hydrometeor vertical profiles.

3.2. Atmospheric Profiles

[16] Without temperature (T), pressure (P), and relative humidity (RH) profiles, radiative transfer calculations cannot be performed. Simulated cloud fields from the Mesoscale Model-5 (MM5) of Hurricane Erin [*Wu et al.*, 2006] were used in this analysis to help generate atmospheric profiles. The MM5 model integration begins at 0000 UTC 7 September 2001 when Erin was an area of disturbed weather and was developed with a resolution of 2.0 km horizontally and ranges between 0.004 and 1.0 km vertically. The MM5 time step closest to the 10 September 2001 at 1700 UTC time is selected for use within this work. The rain rate statistics of the MM5 data (without zero values included) and vertically summed liquid and frozen particle concentrations are provided in Table 1. In order to extract appropriate T, P, and RH profiles, the MM5 computed reflectivity profiles (Z_{sim}) generated by the model were compared to each of the EDOP reflectivity profiles (Z_{obs}) to generate error values (E):

$$E(m) = \sum_{h=o}^{cldtop} |Z_{sim}(i, j, h) - Z_{obs}(m, h)| \quad (3)$$

where m represents the mth of 183 profiles in the flight line, h is an index to the vertical profile, and i, j are indices to the MM5 output. The i, j indices associated with the five most minimum values of E for each m are used to average T and RH profiles of these five MM5 profiles for use in the radiative transfer (RT) calculations.

[17] When these MM5 derived T and RH profiles were used in radiative transfer (RT) calculations of Hurricane Erin it became apparent that the modeled T profile at the upper altitudes was not appropriate. This was determined by reviewing the 55.5 GHz T_B channel that is sensitive to only the upper altitude temperatures. Figure 2b shows that the 55.5 GHz observations are relatively steady across the varying cloud conditions over the flight line. The computations using the MM5 generated T profiles were uniformly warm by about 5K. The inconsistency between the computed T_B using the MM5 T profile and the observations is likely attributable to the coarser vertical resolution for MM5 profiles above 300 mb [*Wu et al.*, 2006]. When the MM5 temperature profiles are allowed to transition to an average (16:47:56 and 17:31:05 UTC) dropsonde profile between 7 to 18 km instead of using the MM5 temperature profiles, the comparison is much better as will be shown in section 5. The problems in getting the calculations of 55.5 GHz to match the observations indicate a disconnect between models and observations. Furthermore, in the hurricane eye only, comparisons with the clear air 10 GHz T_B observed and computed indicated consistently too cold (MM5) computed T_B. In order to compensate for the RH and cloud water, data from dropsonde closest to the eye (1704 UTC) was employed for the temperature, pressure, and relative humidity in the first 7 km nearest the surface.

[18] To reiterate, because the MM5 model simulations cannot absolutely represent the cloud perfectly, dropsonde data is used to provide real constraints on the boundary conditions and profiles. On the other hand, the limited numbers of dropsonde measurements do not provide the variability seen across the flight line observations. Requiring that the reflectivity profiles between the observations and simulations match ensures that hydrometeors exist at the same vertical levels and with nearly the same IWC amounts. The differences in IWC amounts result from differences in the PSDs used to compute reflectivity versus the actual PSDs of the observed profiles (which we do not know). The computed Z for MM5 is not entirely consistent with the PSDs used later, but the modeled reflectivity is

Table 1. MM5 Model Statistics, Zero Values Not Included in Average

Field	Average	Median	Maximum
Surface rain rate, mm h^{-1}	4.8	0.2	19.1
Liquid profile total, g m^{-3}	3.5	0.9	69.5
Ice profile total, g m^{-3}	1.6	0.5	36.1
Surface wind speeds, m s^{-1}	20.09	19.5	44.8

only used to locate common vertical profiles between the modeled data and observed data. Nevertheless, the matched Z profiles along with the dropsonde data constraints provide realistic variations in the temperature, pressure, and relative humidity profiles across the flight line.

3.3. Boundary Conditions

[19] The final step is to insert boundary conditions. For the boundary conditions at the top of the profile, the maximum height level is 18 km near the ER-2 flight altitude. Radiation from the cosmic background is incorporated in the radiative transfer calculations so that the effects of scattering from the ice at the top of the clouds are included. At the Earth's boundary an oceanic surface is assumed since the flight leg is over ocean during the focus times. The RT model requires ocean emissivity and temperature. The ocean temperature was obtained by using equation (3) to average the five closest MM5 surface temperatures. Surface emissivity was more difficult to obtain since it is a function of surface roughness. The average wind speeds emanating from the MM5 data as determined by equation (3) were found to be too weak to produce breaking waves with enough foam to increase emissivity and T_B warming even though Table 1 shows a maximum wind speed of 44 m s^{-1}. This discrepancy was determined using the 10 GHz channel that is sensitive to surface conditions in clear air regions and is caused by equation (3) selecting matching reflectivity profiles that do not necessarily exist at similar distances (and hence wind speeds) from the hurricane eye. The dropsonde wind speeds were greater than those of the MM5 model, and were released at locations within the hurricane (See Figure 1) that permitted easy linear interpolation across the flight line, with a minimum of 8 m s^{-1} in the eye. Using the dropsonde data the wind speeds started at 20 m s^{-1} on the left hand side of the flight path, peaked at 40 m s^{-1} at the left side of the eye, dropped to 8 m s^{-1} in the eye, peaked back to 50 m s^{-1} on the right edge of the eye wall, and then transitioned to 10 m s^{-1} on the rightmost edge of the flight path. The *Monahan and Woolf* [1989] static foam model worked best in generating realistic foam amounts for ocean surface emissivity computations.

4. Particle Habit, Size Distribution, and Parameterizations

[20] The frozen cloud particle contents (IWC in g m^{-3}) derived from the EDOP reflectivities are used with three different frozen habits and associated exponential particle size distributions (PSDs) in order to compute the electromagnetic absorption, scattering, and asymmetry factors of the frozen hydrometeors required for brightness temperature computations. These factors describe how the incident radiation will be absorbed and scattered. The emissive properties of the ocean surface and raindrops are also incorporated. One shape and size parameterization uses a priori in situ data to derive spherical PSDs, while a second parameterization assumes a mixture of dry fluffy spherical snow and graupel particles. The final parameterization assumes a non-spherical three-dimensional bullet rosette of three columns intersecting at orthogonal angles at their center points. The *Marshall and Palmer* [1948] remains constant as the liquid PSD for all three cases.

[21] Since detailed in situ habits and PSDs were not measured for this CAMEX-4 ER-2 flight, the three frozen habits and PSD (or microphysical) parameterizations were selected from published literature and/or measured observations in order to compare how changes in the PSD and habit for frozen hydrometeors affect the computed T_B and the comparison with the observed T_B. While this is a qualitative comparison it still reveals information about the applicability of the different frozen parameterizations with respect to the CAMEX-4 Hurricane Erin observations and different portions of the storm.

[22] All of the three frozen habits employ polydispersive particle size distributions. The bulk absorption and scattering coefficients for each layer and hydrometeor are determined by integrating over the polydispersive particle size distributions. For all parameterizations, the PSD, or number density of the particles within the diameter range D to $D + dD$, is modeled by a decaying inverse exponential function:

$$N(D) = N_0 \exp(-\Lambda D) \tag{4}$$

where N_0 is a multiplier in $m^{-3}mm^{-1}$ and $\Lambda = (2\langle r\rangle)^{-1}$ in mm^{-1} describes the average radius size parameter. At each height interval, the relationship between the bulk (summed) scattering coefficient and bulk absorption coefficient can be used to indicate if radiative cooling from scattering or warming from absorption will dominate. The asymmetry factor describes the direction(s) of scattering with values close to +1 indicating forward scattering, those close to −1 backward scattering, and those at zero indicating isotropic scattering.

[23] To provide proper disclosure, the resultant brightness temperatures are relatively sensitive to the habit, the particle density, the prescribed PSD, and the IWC at each layer. As will be shown later in section 6, the amount of IWC generated through various Z-IWC relationships significantly affects the resultant brightness temperatures. Brightness temperatures are functions of the integrated IWC over the field of view, so changes in IWC are expected to have a large impact. This work does not vary the Z-IWC, habits, and PSDs for the different parts of the hurricane (e.g., convective, stratiform) even though hydrometeors do change in these different regions. To make such changes requires an unavailable robustness in classifying regions and identifying realistic and verifiable Z-IWC, habits, densities, and PSDs for each region.

4.1. Parameterization 1

[24] For this first parameterization, we rely on a priori in situ observations of frozen hydrometeors to derive the particle size distributions. This habit and particle size distribution will be denoted PSD_{IS} where the subscript "IS" for in situ. The Λ value is determined as a function of temperature in the profile and is obtained by curve fitting to ice data from six separate field campaigns, including hurricane observations. (See *Heymsfield et al.* [2006, 2007] for details about the six field campaigns and the data sets.) The Λ_{IS} is:

$$\Lambda_{IS} = \exp(-0.028T)\,\mathrm{mm}^{-1} \tag{5}$$

where T is in degrees Celsius. The frozen hydrometeors are assumed to be spheres with a particle density (ρ_{IS}) that

Table 2. Fitting Coefficients for Equations (12), (13), and (14)

	Scattering Coefficient		Asymmetry Coefficient		Absorption Coefficient 85 GHz	Absorption Coefficient 166 GHz	Absorption Coefficient 183 GHz
A_0	−0.4732	$\mathbf{F_0}$	−0.3464	$\mathbf{B_0}$	1.5E-04	1.1E-04	−6.6E-04
A_1	2.7905	$\mathbf{F_1}$	0.9238	$\mathbf{B_1}$	0.0021	0.0061	0.0153
A_2	−0.7234	$\mathbf{F_2}$	−1.9033	$\mathbf{B_2}$	0.0081	0.0086	−0.0032
A_3	0.8752	$\mathbf{F_3}$	1.5002	$\mathbf{B_3}$	−0.0051	−0.0022	0.0062
A_4	−0.8767	$\mathbf{F_4}$	2.7539	$\mathbf{B_4}$	0.002	5.35E-4	−0.0014
A_5	−3.5739	$\mathbf{F_5}$	−1.8551	$\mathbf{B_5}$	−2.6E-04	−4.8E-05	8.5E-05
A_6	−2.6398	$\mathbf{F_6}$	−3.6527	-	-	-	-
A_7	−0.6078	$\mathbf{F_7}$	−1.2428	-	-	-	-

varies as a function of the diameter. Using the mass to diameter relationship given by *Brown and Francis* [1995], the particle density is defined as

$$\rho_{IS} = 0.00469D^{1.9}/\frac{\pi}{6}D^3\,\mathrm{g\,cm^{-3}}. \tag{6}$$

In this expression, D is in centimeters. The *Brown and Francis* [1995] relationship accounts for both higher and lower moments and provides accurate Z and IWC [*Heymsfield et al.*, 2007]. The ρ_{IS} value for a 0.5 mm, 1 mm, and 5 mm particle are 0.24, 0.11, and 0.02 g cm^{-3}, respectively. The N_0 value is obtained by ensuring that the IWC at each profile height is conserved for the specified Λ_{IS} and ρ_{IS} values integrated for the size distribution of equation (4). The Maxwell-Garnett [*Bohren and Battan*, 1980] dielectric mixing theory is used to obtain the refractive index of these mixed phase (ice and air) particles and then Mie theory is used to determine the absorption, scattering, and asymmetry factors for the RT computations. This parameterization is based on in situ observations and is the most physically consistent with the baseline Z-IWC relationship used to convert EDOP reflectivity to IWC values.

4.2. Parameterization 2

[25] Here the frozen droplets use a 50%–50% combination of fluffy snow and graupel particle PSDs [*Tao and Simpson*, 1993] and will be denoted PSD_{SG}. A mixture of snow and graupel is often seen in hurricane systems [e.g., *Black and Hallett*, 1986], though the 50%–50% mixture may not be applicable throughout all the (convective and stratiform) regions of the hurricane. The snow particles (subscript s) are assumed to be 10% ice and 90% air, while the graupel particles (subscript g) have a fixed 40% ice and 60% air with

$$N_{0s} = 4000.0\,\mathrm{m^{-3}\,mm^{-1}} \tag{7}$$

$$N_{0g} = 8000.0\,\mathrm{m^{-3}\,mm^{-1}} \tag{8}$$

$$\Lambda_{s,g} = \frac{\pi\rho_{s,g}N_{0s,g}}{M}\,\mathrm{mm} \tag{9}$$

where $\rho_s = 0.1 \times 10^6$ g cm^{-3} for 10% ice for snow, $\rho_g = 0.4 \times 10^6$ g cm^{-3} for 40% ice for graupel. The M is the ice water content in g m^{-3} in each cloud layer interval and is divided equally with half allocated for snow and half allocated for graupel. The particles are spherical in shape and use the Maxwell-Garnett [*Bohren and Battan*, 1980] dielectric mixing theory and Mie theory to obtain absorption, scattering, and asymmetry factors.

4.3. Parameterization 3

[26] This third parameterization has a habit similar to a bullet rosette with three cylinders intersecting orthogonally at their midpoints and is denoted PSD_{C3}. Rosettes do not typically appear in hurricanes [*Black and Hallet*, 1986], however, this study uses the rosette to represent non-spherical particles. It would be preferable to assume an aggregate habit, but the relationships between the physical properties and radiative properties of aggregates are not well known and are only beginning to be researched. The rosette habit used herein was described by *Kim* [2006], with the single cylinder aspect ratio from *Auer and Veal* [1970] and *Kim et al.* [2007]:

$$D = 0.197L^{0.414}\,(\mathrm{mm}) \tag{10}$$

where L is the length and D is the diameter of the column. The Λ in equation (4) for the non-spherical particles is equation (5) and is quite appropriate for frozen hydrometeors in clouds [*Brown and Francis*, 1995]. The maximum size of the particle size distribution is fixed by *Kim* [2006] requiring that the size parameter ($\pi D_{eff}\ \lambda^{-1}$) <2.5 where λ is the operational wavelength and D_{eff} which is the effective diameter of a spherical particle with volume given by the three intersecting cylinders. Note that we plotted *Kim*'s [2006] provided curve fits and determined that they were good up to size parameters of 3.5. Thus the maximum L for this PSD is 7 mm. While it is doubtful that rosettes would attain the size of 7 mm, we use them to be representative of non-spherical particles that do become that large.

[27] The volume for the 3 cylinder habit is given by:

$$V = \frac{3}{4}\pi D^2 L - \sqrt{2}D^3 \tag{11}$$

where the intersecting center volume is removed for two of the cylinders. The habit shape and aspect ratio fixes the volume in each individual particle such that given the maximum diameter the total ice water content in each layer can be partitioned into an exponential particle size distribution and N_0 can be determined using equations (11) and (4). The increment in the L dimension for the particle size distribution is 0.1 mm.

[28] To compute the absorption, scattering, and asymmetry parameters for frequencies less than 80 GHz for the

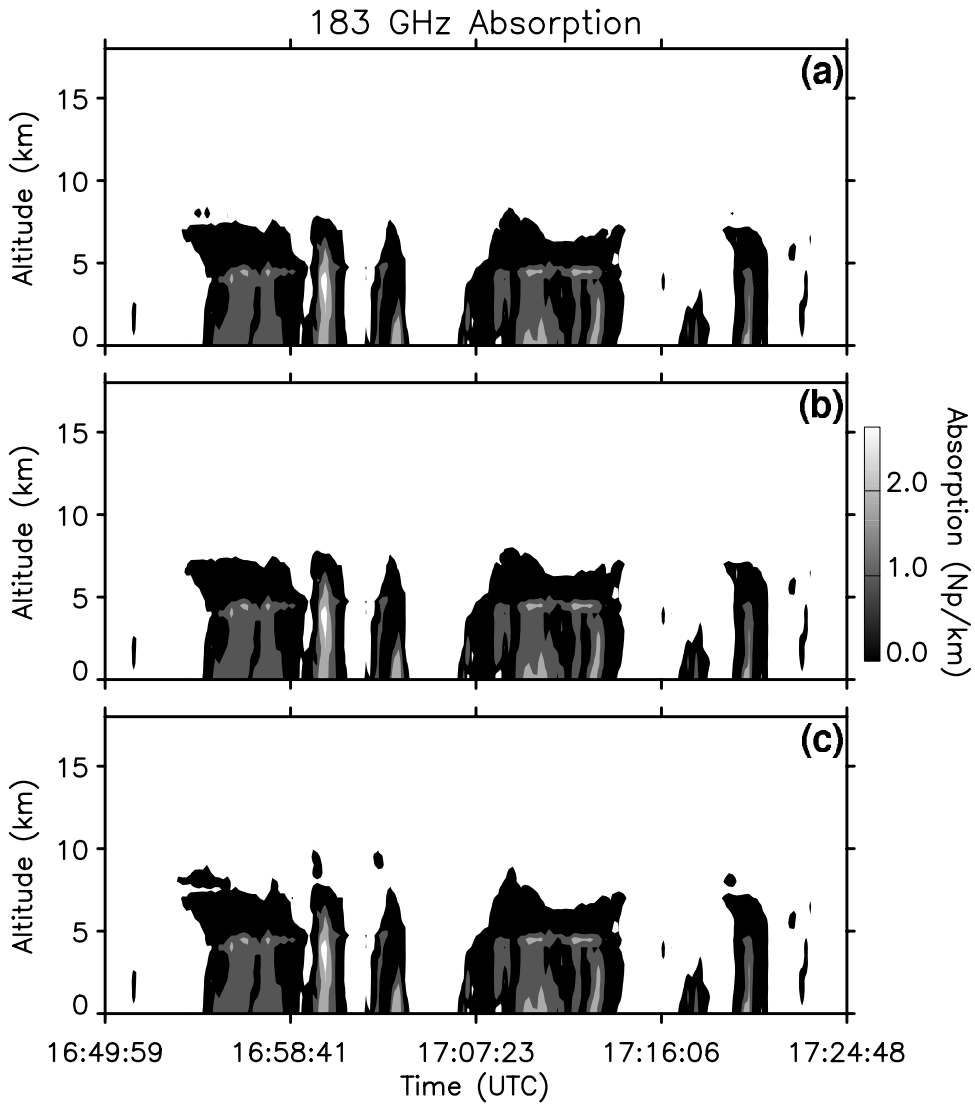

Figure 4. Bulk absorption fields at 183 ± 7 GHz for (a) PSD_{SG}, (b) PSD_{IS}, and (c) PSD_{C3}. Shading thresholds are at 0.1, 0.5, 1.0, and 2.0 nepers/km.

PSD_{C3}, spheres and Mie theory is used [*Kim*, 2006]. For frequencies above 80 GHz, dielectric mixing theories are not used, instead, the discrete dipole approximation is used [*Draine and Flatau*, 1994] with the bullet rosette habit. The procedure is similar to that described by *Kim* [2006] and the DDA curve fit coefficients for this aspect ratio are provided in Table 2. The curve fit equations are from *Kim* [2006] and are reproduced here:

$$\log_{10}\left(\frac{C_{scat}}{\pi r_{eff}^2}\right) = \sum_{n=0}^{7} A_n (\log_{10} x)^n \tag{12}$$

$$\frac{C_{abs}}{\pi r_{eff}^2} = \sum_{n=0}^{5} B_n x^n \tag{13}$$

$$\log_{10}(g) = \sum F_n (\log_{10} x)^n. \tag{14}$$

With these equations and relationships the scattering, absorption, and asymmetry radiative properties can be computed for the three parameterizations as described in the next section.

5. Radiative Transfer Calculations

[29] An accurate and efficient radiative transfer (RT) model is required to transform the microphysical information into upwelling passive microwave brightness temperatures (T_B) that are then compared to the AMPR and HAMSR observations. The radiative transfer model used in this work is a planar-stratified scattering based model originally developed by *Gasiewski* [1993] and modified as described by *Skofronick-Jackson et al.* [2003]. The RT model used herein allows for multiple scattering among the six different hydrometeor types (i.e., suspended cloud water, rain, suspended cloud ice, snow, hail, and graupel). In this work only rain and snow are allowed, though the size distributions for rain and snow extend down to sizes

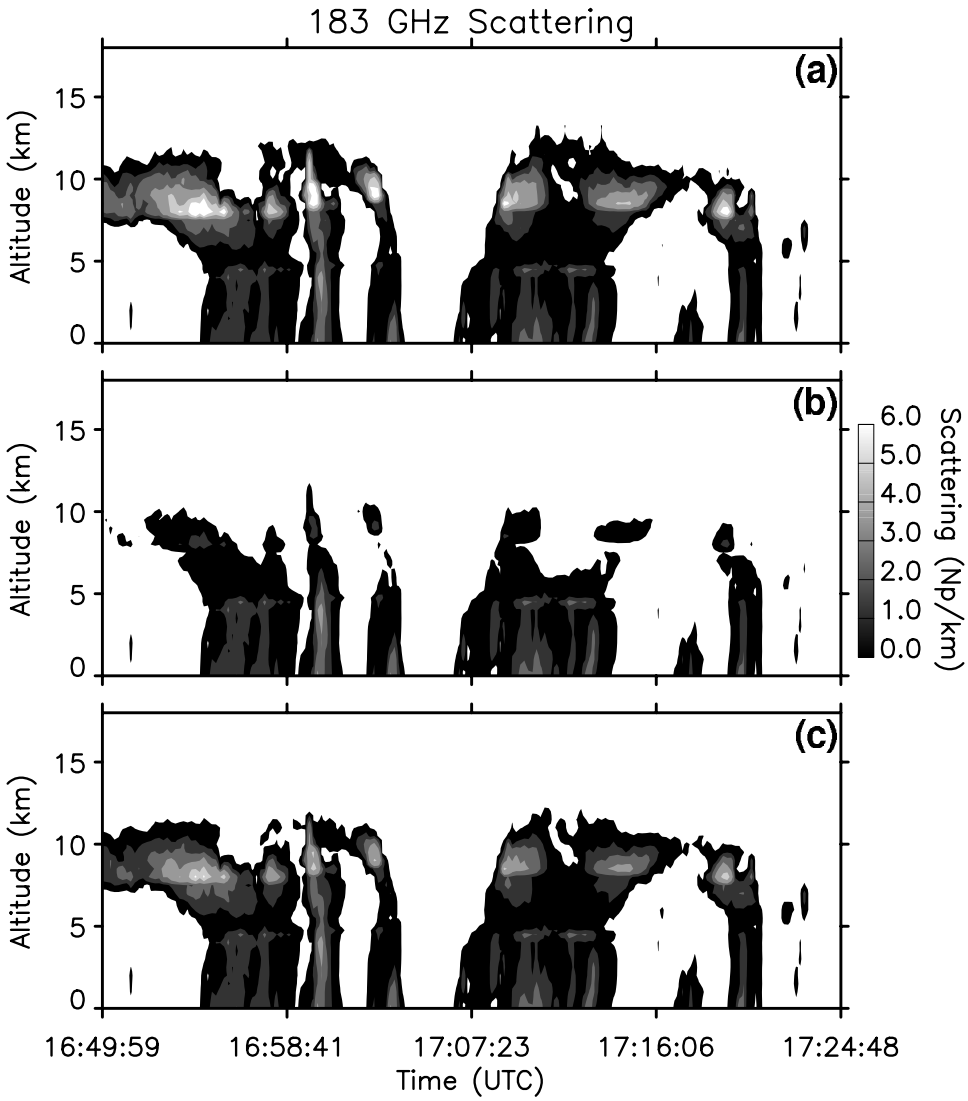

Figure 5. Bulk scattering fields at 183 ± 7 GHz for (a) PSD_{SG}, (b) PSD_{IS}, and (c) PSD_{C3}. Shading thresholds are at 0.1, 0.5, 1.0, 2.0, 4.0, and 6.0 nepers/km.

appropriate for cloud water and cloud ice. Flexibility exists in that the user can select observation height, viewing angle, frequency (tested from 6 to 425 GHz) and polarization. The RT model requires as input instrument specifications, vertical profiles of temperature, height, relative humidity, and PSDs of the hydrometeors in the cloud or their radiative properties. It is assumed that a planar stratified RT model is acceptable in this work since only high resolution nadir observations are used in the retrieval. Furthermore, since only nadir observations are analyzed in this work, any polarization sensitivity due to nonspherical particles is minimized.

[30] Within the radiative transfer numerical procedure there are settings and assumptions that add uncertainty to the calculated values, but these add less uncertainty as compared to assumptions in the hydrometeor profile [*Kim et al.*, 2004]. Further, while it would be a useful study to determine how uncertainties scale up to affect the calculated brightness temperatures, such a study requires a different analysis than used in this work and would be best provided in a future paper.

[31] Once individual absorption, scattering, and asymmetry factors have been computed for each shape as described in section 4, they are integrated over polydispersive PSDs as described by *Gasiewski* [1993] to obtain the bulk absorption, scattering, and asymmetry factors over the vertical structure of the hurricane flight line. Figure 4 shows the bulk absorption coefficients for the three different frozen habits and parameterizations at 183 ± 7 GHz. There is essentially no difference in the absorption profiles since the Marshall-Palmer PSD for rain was not changed and frozen hydrometeors do not contribute much to the absorption coefficient. For the scattering profiles of 183 GHz, the PSD_{SG} (Figure 5a) and PSD_{C3} (Figure 5c) tend to produce more scattering for a larger vertical extent than the PSD_{IS} (Figure 5b). Scattering is increased for the PSD_{SG} and PSD_{C3} by their relatively large particle size, larger N(D), and more dense (ρ) particles at those larger sizes. For the PSD_{IS} particles, scattering is reduced due to the less dense particles at larger sizes (Figure 5b).

[32] The asymmetry parameters at 183 ± 7 GHz (and for each frequency) play an important role in the resulting

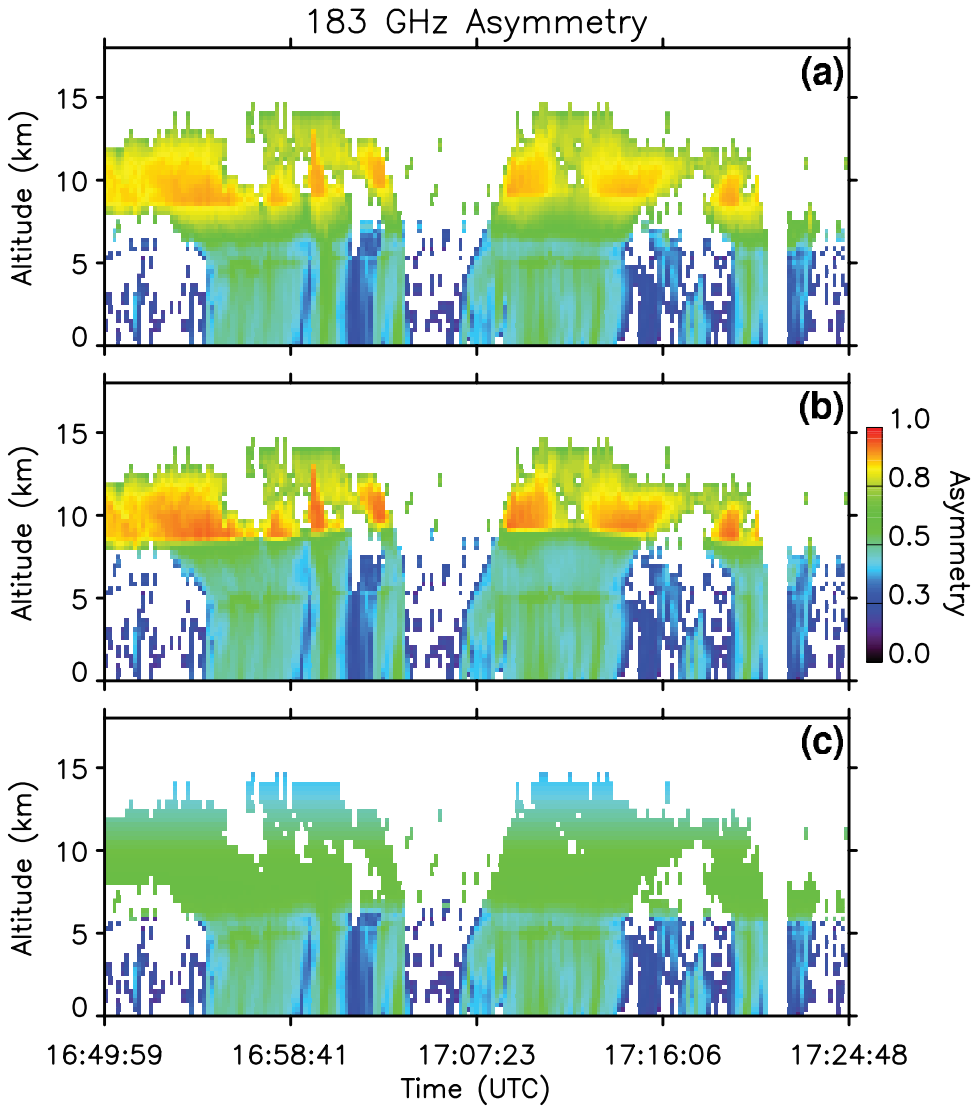

Figure 6. Bulk asymmetry fields at 183 ± 7 GHz for (a) PSD_{SG}, (b) PSD_{IS}, and (c) PSD_{C3}. Asymmetry factors are unitless.

brightness temperature. The asymmetry factors are highly dependent on the frequency, refractive index, size, and temperature of the particles [*Gasiewski*, 1993]. In turn, the refractive index is dependent on the particle habit. The PSD_{SG} particles have asymmetry in the 0.8 range in the ice layers (Figure 6a) because they are large spheres with $\rho_s = 0.1$ and $\rho_g = 0.4$. For PSD_{IS} spheres, the asymmetry is above 0.9 for the highest altitudes (Figure 6b) and closer to 0.5 in the mid-altitude range because the largest particles in PSD_{IS} are low density ($\rho \ll 0.1$). For the PSD_{C3} case, the asymmetry factors are near 0.4 to 0.6 in most of the liquid and frozen parts of the vertical profile (Figure 6c). Here the rosette habit suppresses the generation of higher asymmetry factors. Since an asymmetry factor determines the direction(s) of scattering, it works with the absorption and scattering coefficients in numerically computing the brightness temperature.

[33] At 85 GHz, the absorption fields for the three parameterizations are as equivalent as in the 183 GHz case and not shown in a figure. On the other hand the scattering profiles (Figure 7a, 7c) show that the PSD_{SG} and PSD_{C3} parameterization have scattering in the ice layers and it is rather intense in the PSD_{SG} case. In Figure 8, the 85 GHz asymmetry shows a pattern similar to the 183 GHz asymmetry but at lower and more isotropic values.

[34] Although not shown, the absorption, scattering, and asymmetry factors have similar patterns for 166 GHz as at 183 GHz. At 10 GHz the asymmetry factor ranges between −0.05 and 0.2 for all three frozen habits. This means that any 10 GHz scattering (less than ~0.05 neper km^{-1} for all habits) is more isotropic, however at 10 GHz the strong absorption coefficient (to 0.3 neper km^{-1} for all habits) overpowers the weak scattering signal.

6. Comparison Between Observed and Computed Brightness Temperatures

[35] The radiative transfer model along with the computed bulk radiative data were used to compute brightness temperature values for the three ice parameterizations. Prior

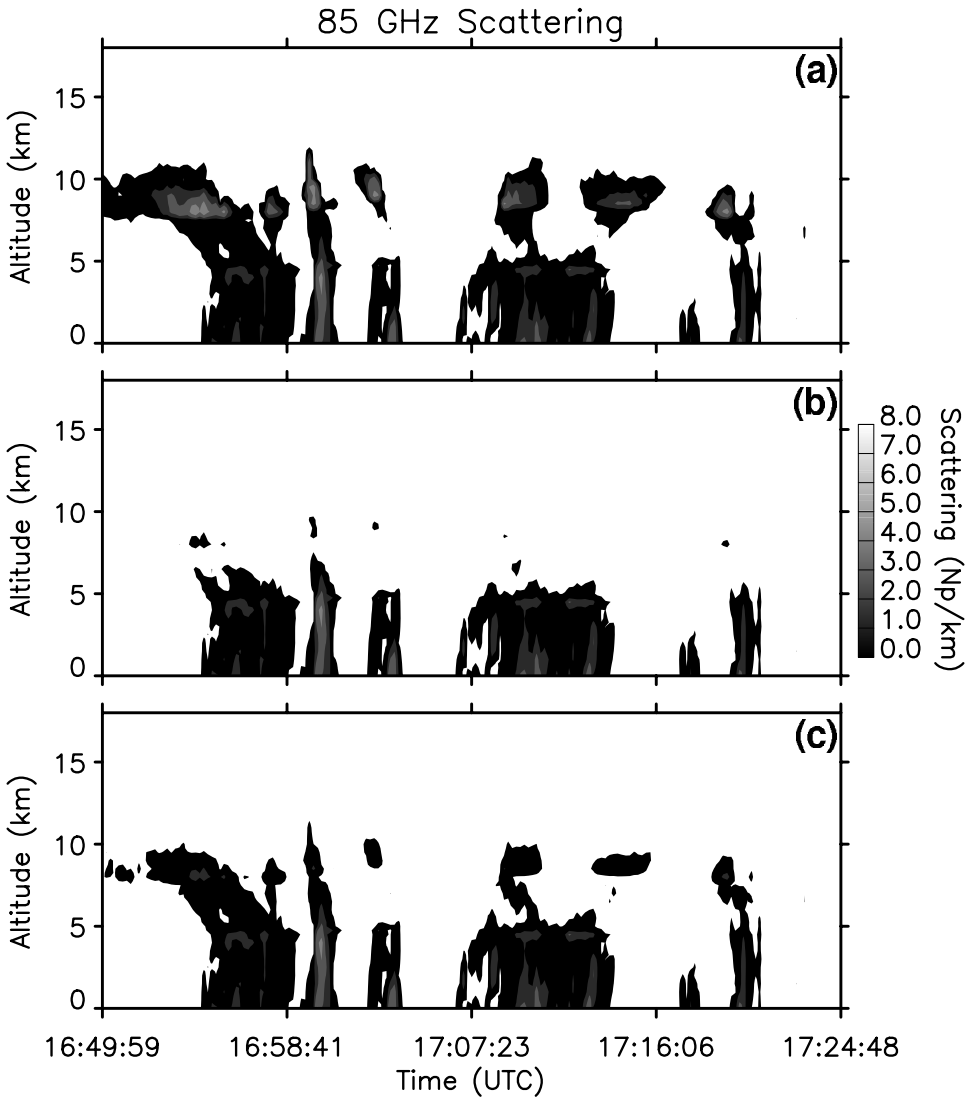

Figure 7. Bulk scattering fields at 85 GHz for (a) PSD_{SG}, (b) PSD_{IS}, and (c) PSD_{C3}. Shading thresholds are at 0.1, 0.5, 1.0, 2.0, 4.0, 6.0, and 8.0 nepers/km.

to comparing observations to the calculations, a review of Figures 2a–2d will show that the cloud structures and T_B values are quite variable in several sections of the ER-2 flight line, though in the hurricane eye all three parameterizations produce equivalent computed brightness temperature values. It would be best to tune the habit and size distribution parameters for the inner and outer rainbands, and convective/stratiform regions of the hurricane since many investigators have noted different frozen hydrometeors in these various regions [*Heymsfield et al.*, 2006; *Black and Hallett*, 1986]. However, robust classification schemes and further, an adequate understanding of realistic and appropriate habits and size distributions are not easily obtained, nor warranted in this study.

[36] The comparisons between computed and observed brightness temperatures are found in Figures 9 and 10. In general, the PSD_{IS} particles did not produce enough scattering and proper asymmetry directions to reduce calculated brightness temperatures to the lower observed values at the higher frequencies. The non-spherical rosettes (PSD_{C3}) managed to reasonably capture the observed AMSR and HAMSR brightness temperatures, though the PSD_{SG} performed better at 85 GHz (Figure 9e). Table 3 shows that the correlation coefficients between the observations and PSD_{SG} and PSD_{C3} for each frequency are larger than the correlations between the observations and the PSD_{IS}. In the following paragraphs the results for the different parameterizations will be discussed for each plotted frequency. Later, comparisons for two additional Z-IWC relationships will be discussed.

6.1. Comparisons by Frequency

[37] For 10 GHz, all three parameterizations track the observations along the flight line reasonably well and are within ~10 K except in the eye of Hurricane Erin (Figure 9a). The mean differences between the observations and the three parameterizations all are around 2.0 Kelvin (Table 3). For 19 GHz (Figure 9b), there is a similar response as for 10 GHz except that the 19 GHz calculations are too cool by a mean ~5 K difference. For 19 GHz, brightness temperature calculations near the regions of a clearly defined radar bright band (horizontal red lines in Figure 2a) are depressed with respect

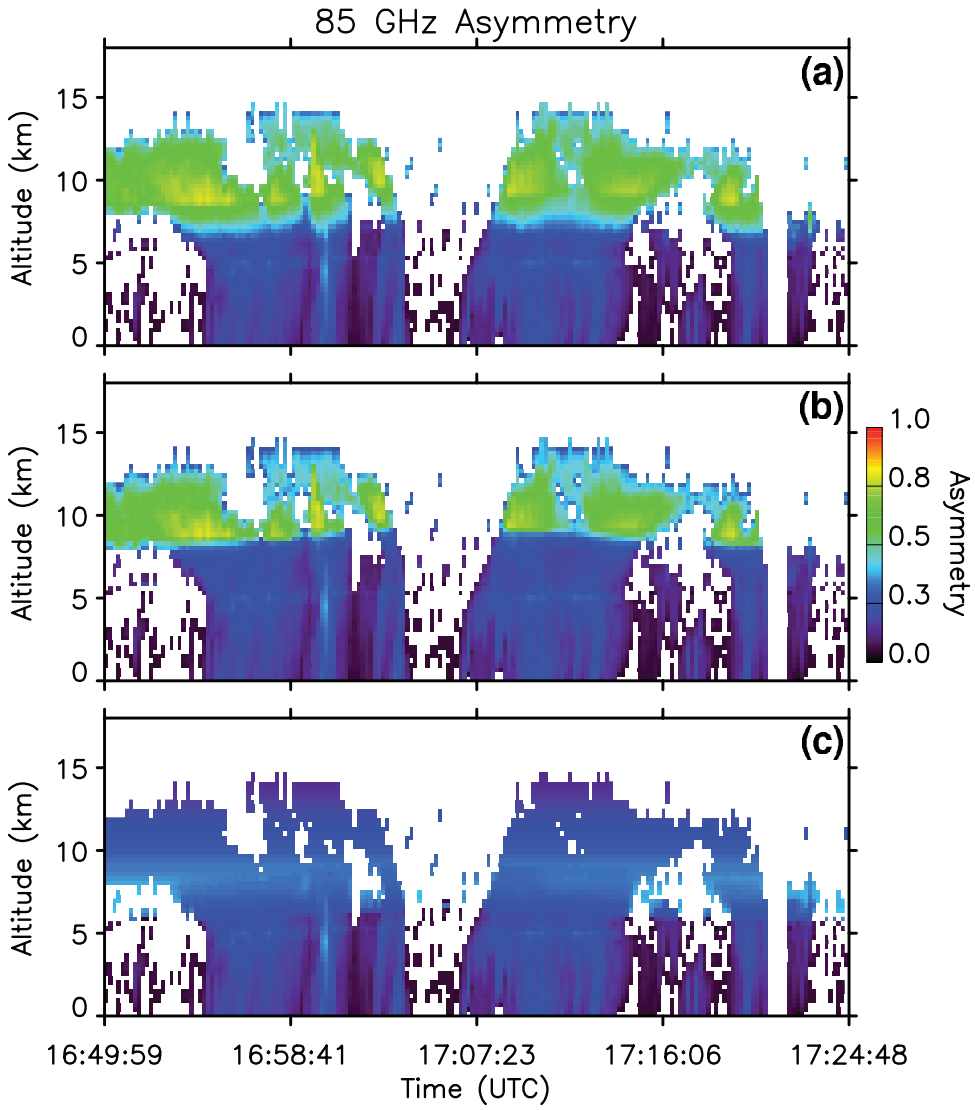

Figure 8. Bulk asymmetry fields at 85 GHz for (a) PSD_{SG}, (b) PSD_{IS}, and (c) PSD_{C3}. Asymmetry factors are unitless.

to the observations. This may indicate that the Marshall-Palmer PSD used for rain and/or the vertical transitions between all rain and all ice are inadequately modeled. For 19 GHz adding a melting layer would warm the T_B values by 2–3 Kelvin [*Skofronick-Jackson et al.*, 2002] which would be useful in these bright band regions. For 37 GHz (Figure 9c), the calculations for all parameterizations track the observations, except near the Hurricane Erin's eye (as for 10 and 19 GHz). For 37 GHz, adding a melting layer would have the largest impact where T_B values are increased by up to 5–15 K [*Skofronick-Jackson et al.*, 2002] which would bring the mean difference between the calculations and observations closer to zero (Table 3).

[38] For 55.5 GHz the brightness temperature observations do not change by more than 5–6 Kelvin across the whole flight line due to the fact that this channel is sensitive to temperatures high in the atmosphere, closest to the ER-2 aircraft. Since the sensitivity altitude exists above any hydrometeors, there is little response of this channel to hydrometeors. As noted in section 3.2, the MM5 generated T profiles were replaced by the colder profiles from the dropsondes. This was required to get the 55.5 GHz T_B calculations closer to the observations.

[39] For 85 GHz in Figure 9e, brightness temperatures from the three parameterizations show more deviations. This is expected since the three parameterizations differ only in their frozen particle characteristics and 85 GHz is responsive to frozen hydrometeor characteristics. The mean differences for the computed minus the observed T_B values are 25, 12, and 20 for PSD_{IS}, PSD_{SG}, and PSD_{C3}, respectively. The PSD_{IS} has large diameter, low density particles such that scattering above the melting layer is almost nonexistent (Figure 7b), yet it has a high asymmetry above the melting layer (Figure 8b). Thus the warming from low altitude absorption is scattered upward in a forward asymmetry direction into the radiometer, producing warm T_B values for PSD_{IS}. On the other hand, the PSD_{C3} has more scattering at upper layers in the cloud (Figure 7c), with an isotropic asymmetry direction. Thus warming from absorption and the ice scattering mix isotropically to produce

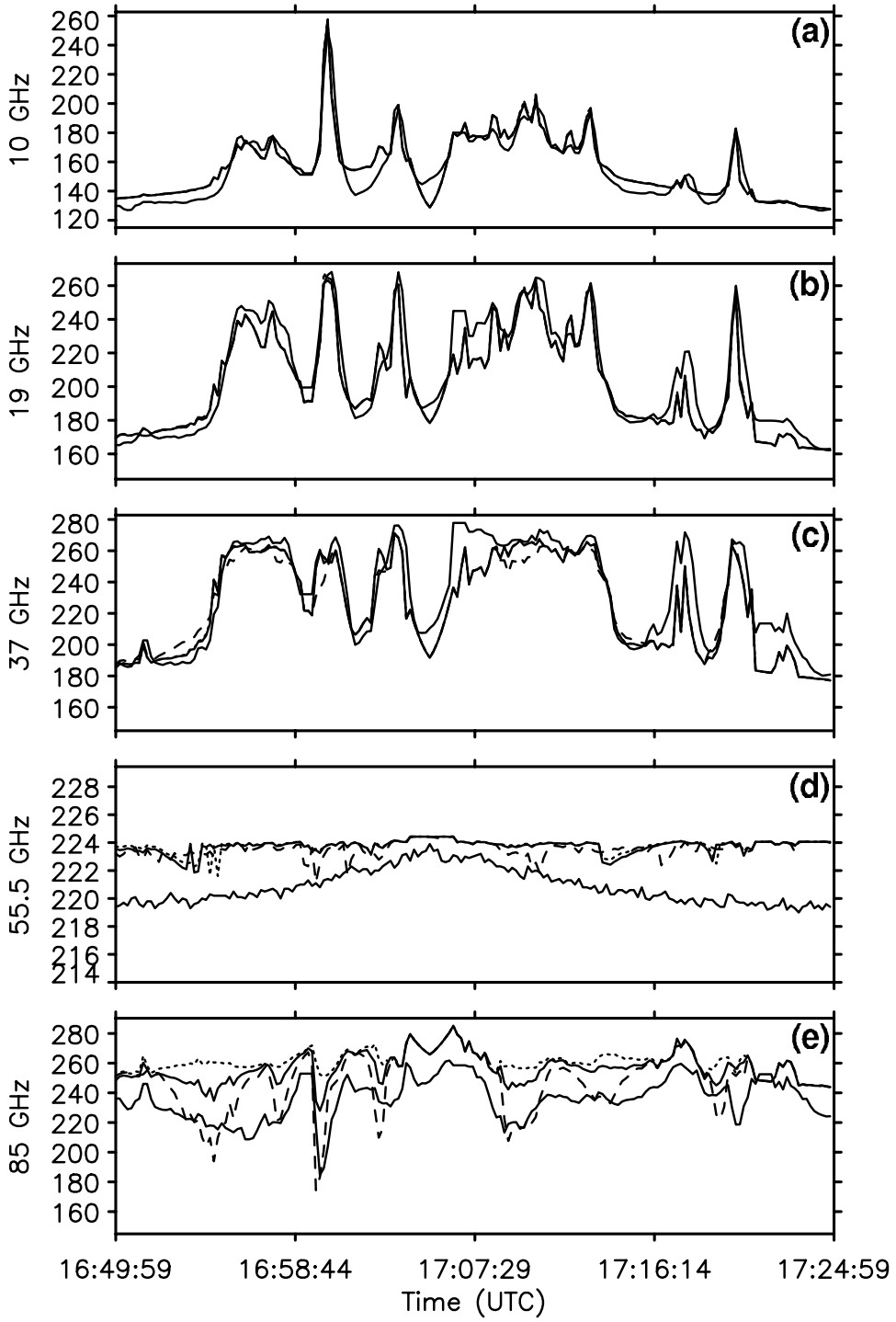

Figure 9. Brightness temperature values for (a) 10, (b) 19, (c) 37, (d) 55.5, and (e) 85 GHz in Kelvin for the observations (solid line), PSD_{SG} parameterization (dashed line), PSD_{IS} parameterization (dotted line), and PSD_{C3} parameterization (dash-dotted line).

reductions in T_B values (Figure 9e). Finally, PSD_{SG}, have even higher high attitude scattering that over powers the low altitude absorptive warming, such that T_Bs are much closer to the observations. It is likely that adding a melting layer would increase T_B values by ~5–10 K [*Skofronick-Jackson et al.*, 2002] which is the wrong direction of change if the goal is to cool calculations to match the observations.

[40] In Figure 10a, the 166 GHz channel image is shown. The 166 GHz channel is a window channel like 85 GHz, however it responds to frozen hydrometeors of a smaller size and at a higher altitude than those sensed by the 85 GHz channel due to its smaller operating wavelength. For the 166 GHz channel, the rosette habit and its PSD produces a better match to the observations than do the other parameterizations as evidenced by its slightly higher correlation coef-

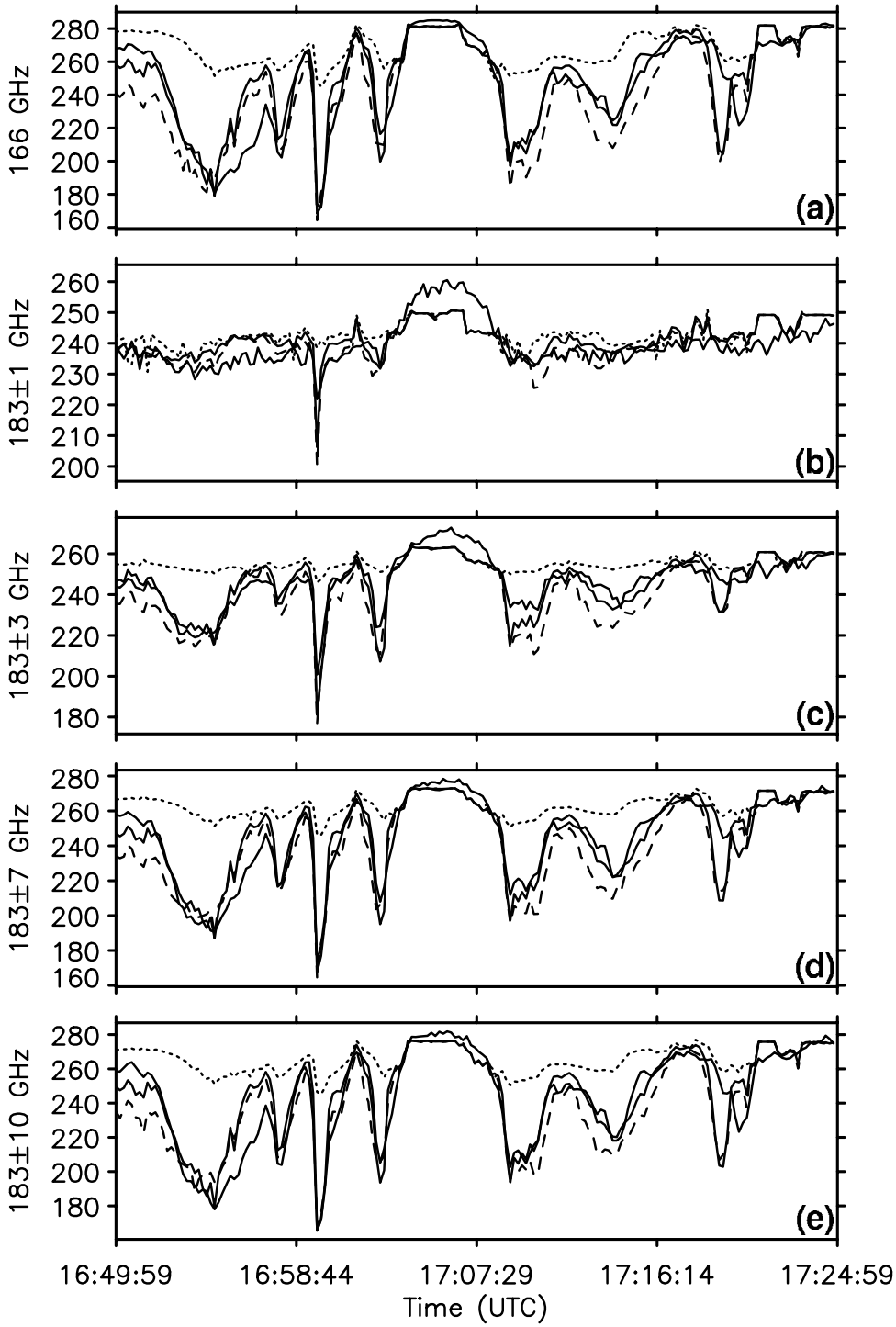

Figure 10. Same as Figure 9 except for (a) 166, (b) 183.3 ± 1, (c) 183.3 ± 3, (d) 183.3 ± 7, and (e) 183.3 ± 10 GHz.

ficient and smaller mean difference (Table 3). The PSD_{SG} case is not far behind the PSD_{C3} case for 166 GHz.

[41] In each of the comparisons between observation and calculations for the 183 GHz channels (Figures 10b–10e), the parameterizations having a larger particle density (PSD_{SG} and PSD_{C3}) have a better match to the observations (Figures 10b–10e and Table 3). The PSD_{SG} mean differences (Table 3) are colder than the PSD_{C3} differences by 4–5 Kelvin. This indicates a slight advantage of PSD_{C3} in matching the observed brightness temperatures; however, a different mixture of snow and graupel (other than the 50%–50% mixture used herein) would change the computed brightness temperatures. The fluffy PSD_{IS} particles do not provide enough scattering and proper asymmetry directions at these higher frequencies for the same reasons as discussed for 85 GHz. Using dielectric mixing models [e.g., *Bohren and Battan*, 1980] for the higher frequencies for the less dense spheres (PSD_{IS}) seemed to produce inappropriate

Table 3. Correlation Coefficients and Mean Values Between the T_B Observations and the Three Sets of Computed T_B Values Using the CRYSTAL-FACE IWC = $0.103Ze^{0.33}$ Relationship

	Obs. − PSD_{IS}		Obs. − PSD_{SG}		Obs. − PSD_{C3}	
Freq., GHz	Mean	Correlation	Mean	Correlation	Mean	Correlation
10	1.81	0.94	2.00	0.94	1.75	0.94
19	−5.37	0.94	−5.21	0.94	−5.45	0.94
37	−7.27	0.92	−7.82	0.91	−7.43	0.92
85	25.10	0.54	12.19	0.74	20.80	0.76
50	−5.76	0.86	−9.23	0.80	−6.48	0.88
52	−3.09	0.89	−7.88	0.68	−3.82	0.92
55	2.96	0.35	2.72	0.18	2.92	0.36
166	20.73	0.82	−5.76	0.85	2.31	0.89
183 ± 1	3.31	0.65	0.47	0.72	1.78	0.70
183 ± 3	8.26	0.78	−5.60	0.89	−1.36	0.90
183 ± 7	17.49	0.82	−5.44	0.89	0.08	0.92
183 ± 10	21.37	0.83	−3.68	0.87	1.97	0.90

electromagnetic characteristics. For example, the fluffy particles represented by effective medium mixing models had large asymmetry factors in the frozen parts of the cloud (Figure 6a, 6b) for the PSD_{SG} and PSD_{IS}. As stated previously, the asymmetry factor is a function of the particle shape, size, temperature, and ice-air-water composition (i.e., habit) and determines the direction(s) of scattering from a hydrometeor. Large asymmetry factors increased forward scattering of the radiation from the warm lower layers so that computed brightness temperatures were too warm if there is little or no competition from ice scattering. While PSD_{SG} had large asymmetry factors (Figure 6a) it also had large scattering (Figure 5a). On the other hand, the PSD_{IS} had high asymmetry (Figure 6b), but low ice scattering (Figure 5b), thus the warming from liquid absorption was able to forward scatter into the down-looking radiometer without ice scattering interfering. The C3 rosette shape along with the discrete dipole approximation produced the scattering and asymmetry factors that led to the T_B computations closest to the observations in terms of mean differences as seen in Table 3, though the PSD_{SG} computations were very close to the PSD_{C3} values. Adding additional Hurricane Erin data sets will not change the results described above because the brightness temperature differences are driven by the three remarkably distinct shape and size parameterizations.

6.2. Comparisons by Z-IWC Relationship

[42] Since the Z to IWC relationships are fraught with uncertainty, two additional Z-IWC relationships were implemented and the brightness temperatures recomputed using the PSD_{SG}, PSD_{IS}, and PSD_{C3} parameterizations. This comparison showed that by far, the selection of the Z-IWC relationship has the largest role in determining the resulting brightness temperature values. The two additional Z-IWC relationships were obtained by curve fitting (1) Hurricane Humberto data from the CAMEX-4 field campaign [*Heymsfield et al.*, 2006], and (2) six field campaigns of Z and IWC observations [*Heymsfield et al.*, 2007]. The resulting curve fits produce equation (2) coefficients of $a_{Humb} = 0.102$, $a_{all} = 0.066$, and $b_{Humb} = 0.57$, $b_{all} = 0.44$.

[43] As a method of comparison, Figure 11 shows the 166 through 183 GHz brightness temperature comparisons for the Hurricane Humberto derived Z-IWC relationship. The significant decrease in computed brightness temperatures for the PSD_{SG} and PSD_{C3} cases are caused by the increase in the IWC amounts and hence the scattering coefficients. Again the highly fluffy low-density PSD_{IS} spheres do not produce enough scattering to cool the brightness temperatures. The correlation coefficients and mean differences between the observations and the brightness temperatures obtained using the Hurricane Humberto relationships are provided in Table 4. The mean difference values in Table 4 show increased negative values with respect to Table 3 of the PSD_{SG} and PSD_{C3} cases reiterating the reduction in computed brightness temperatures with respect to the observations.

[44] Combining the six field campaign data sets reported by *Heymsfield et al.* [2007] produces brightness temperature values in between those of the Hurricane Humberto case and the baseline CRYSTAL-FACE Z-IWC relationship. These results are reported in Table 5. As a simple explanation, the decreases in computed brightness temperature may be related to the b exponent in equation (2). As b increases, computed brightness temperatures decrease, but only assuming appropriate habits (more dense particles) and PSDs. Clearly, more field observations are needed to derive physically and radiatively consistent relationships between the reflectivities, habits, PSDs and absorption, scattering, asymmetry, and backscattering coefficients.

7. Summary and Conclusions

[45] This work was undertaken in order to evaluate the relationships between frozen cloud particles and their radiative signatures for developing and improving algorithms for retrievals of ice particle characteristics. In summary, three different ice parameterizations were used to compute brightness temperature values to compare with observations from CAMEX-4 radiometers on the ER-2 aircraft. In order to initialize the cloud profiles used in the radiative transfer calculations, the radar reflectivities taken from the EDOP instrument on the ER-2 were converted to mass contents at 0.25 km interval levels from the surface to 18 km in the vertical profile. A baseline Z-IWC relationship was derived from observed reflectivities and IWC during the CRYSTAL-FACE field campaign. The EDOP reflectivities were compared to Hurricane Erin MM5 modeled reflectivities to extract and average the five closest atmospheric profiles such that the MM5 profiles of temperature, pressure, and relative humidity and surface conditions were available across the ER-2 flight path data set. Using dropsonde data, some modifications to the modeled data were used to improve surface characteristics and upper altitude temperature profiles.

[46] With the profile database generated by the EDOP instrument, dropsondes, and the Hurricane Erin MM5 model, brightness temperatures were computed for three ice habit and particle size parameterizations. The liquid drops followed the *Marshall and Palmer* [1948] PSD throughout all parameterizations. The PSD_{SG} ice parameterization relied on a modified *Marshall-Palmer* PSD composed of 50% spherical snow particles and 50% spherical graupel particles of fixed ρS and ρG; the PSD_{IS} parameterization was derived from in situ observations of ice clouds and used a variable ρ as a function of diameter, while the PSD_{C3} parameterization was of a non-spherical bullet

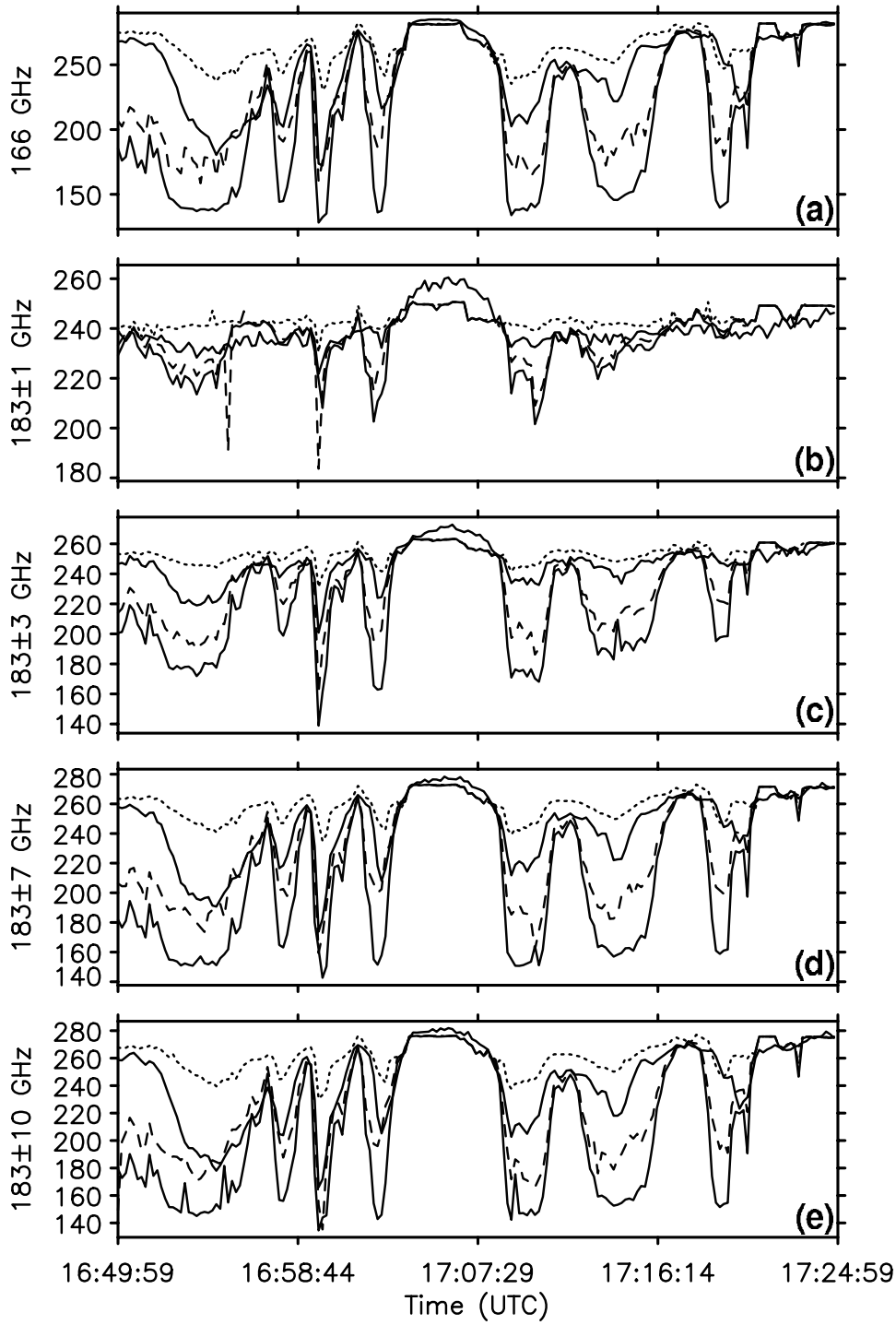

Figure 11. Same as Figure 10 except that the Hurricane Humberto derived Z-IWC relationship is used to obtain the IWC profiles prior to the brightness temperature calculations.

rosette particle of three intersecting cylinders. In comparing the observations to the calculations, the overall best fit resulted from the rosette particles of three intersecting cylinders, though the PSD_{SG} was better at 85 GHz and not far behind the PSD_{C3} case for the other frequencies. The mismatch of the PSD_{IS} parameterizations indicates inadequate modeling of their scattering and asymmetry electromagnetic characteristics due to low particle densities.

[47] As would be expected, the lower frequency AMPR observations (10 to 19 GHz) had essentially no difference among the three parameterizations (Figures 9a and 9b). These channels are mostly responsive to the liquid particles in the cloud and the parameterizations discussed herein only made changes to the frozen droplets. At 37 GHz (Figure 9c), we expect and note a response to both liquid and frozen hydrometeors. The 50–60 GHz temperature profiling channels (Figure 9d) of the HAMSR instrument are responsive

to hydrometeors in the cloud except at the higher frequencies close to 60 GHz that sense only high altitude atmospheric temperatures. The 183 GHz channels (Figures 10b–10e) are sensitive to both atmospheric water vapor and the frozen droplets in the cloud. For these high frequencies, both the PSD_{SG} and PSD_{C3} produced acceptable brightness temperatures as compared to the observations (see Table 3).

[48] As a test of sensitivity to the Z-IWC relationship, two additional reflectivity and ice water content relationships were derived using data from (1) Hurricane Humberto, and (2) six field campaigns. The resulting comparison of the computed brightness temperatures shows that, indeed, the initialization of the IWC profiles plays a primary role in the resulting computed brightness temperatures (assuming acceptable assumptions for habit and PSD). This means that if the Z to IWC retrieval is not appropriate then selecting the best habit and PSD relationship becomes more difficult.

[49] The three most significant findings of this work are summarized here. The first finding was that the MM5 cloud model output required adjustments to produce matches for the clear air brightness temperature observations. The second significant finding revealed the importance of the bulk asymmetry parameter (that describes the direction of scattering) in the resultant T_B values. Typically, passive remote sensing has attributed T_B values to the combination of the bulk absorption and scattering parameters, essentially ignoring the role of the asymmetry. The third finding was that combination of the initial IWC profiles, along with the absorption, scattering, and asymmetry radiative properties derived from the IWC profiles and used in the radiative transfer calculations all work together to produce brightness temperature values. Thus care to ensure physical and radiative consistency in measuring and analyzing future field campaign data sets is paramount.

[50] This work has shown that the full channel spectrum of electromagnetic properties of frozen hydrometeors can be modeled using particles with larger ρ values or non-spherical ice particle parameterizations and that the bulk asymmetry factor along with the scattering plays a big role in the resultant computed high frequency brightness temperatures. In reality, multiple habit and PSD models should be necessary for a more complete vertical cloud profile and may help with the 85 GHz discrepancies. These physical models of frozen hydrometeors will depend on many factors such as vertical location and atmospheric temperature, method of forming and re-freezing, and ice-air-water ratios. Detailed in situ observations and reliable cloud resolving models for the ice phase particles are required and currently underway in order to develop and validate appropriate and more realistic frozen particle parameterizations. Discrete dipole approximations or other methods can then be used to convert physical properties to absorption, scattering, and asymmetry properties for radiative transfer calculations and this seems to help with avoiding the problems plaguing conversions of in situ measurements of frozen hydrometeors to fluffy spherical particles. Meanwhile this work shows that some early non-spherical models such as the non-spherical bullet rosette with three intersecting cylinders can produce brightness temperatures comparable to wide-band passive observations from 10 to 183 GHz, though other habit and parameterizations produce acceptable brightness temperature values as well. Future work should and will focus on deriving relationships between the in situ observed properties of particle habit, PSD, and IWC and the radiatively observed properties of absorption, scattering, asymmetry, (for passive radiometer observations) and back-scattering (for active radar observations).

Table 4. Correlation Coefficients and Mean Values Between the T_B Observations and the Three Sets of Computed T_B Values Using the Hurricane Humberto IWC = $0.102Ze^{0.57}$ Relationship

	Obs. – PSD_{IS}		Obs. – PSD_{SG}		Obs. – PSD_{C3}	
Freq., GHz	Mean	Correlation	Mean	Correlation	Mean	Correlation
10	1.90	0.94	2.48	0.94	2.01	0.94
19	−5.18	0.94	−6.30	0.91	−5.13	0.94
37	−6.70	0.91	−19.50	0.61	−8.48	0.92
85	23.71	0.66	−9.53	0.68	−4.44	0.68
50	−5.67	0.84	−28.08	0.35	−12.61	0.76
52	−3.63	0.88	−25.03	0.46	−10.66	0.59
55	3.00	0.33	2.20	0.09	2.73	0.20
166	15.33	0.66	−18.93	0.77	−36.64	0.76
183 ± 1	3.98	0.68	−1.89	0.65	−4.09	0.64
183 ± 3	6.52	0.88	−13.45	0.85	−23.49	0.84
183 ± 7	13.64	0.75	−15.84	0.81	−32.48	0.81
183 ± 10	17.73	0.91	−15.69	0.78	−32.17	0.78

Table 5. Correlation Coefficients and Mean Values Between the T_B Observations and the Three Sets of Computed T_B Values Using the IWC = $0.066Ze^{0.44}$ Relationship Derived From Six Field Campaigns of Data

	Obs. – PSD_{IS}		Obs. – PSD_{SG}		Obs. – PSD_{C3}	
Freq. (GHz)	Mean	Correlation	Mean	Correlation	Mean	Correlation
10	1.83	0.94	2.00	0.94	1.87	0.94
19	−5.36	0.94	−5.18	0.94	−5.30	0.94
37	−7.21	0.92	−8.29	0.89	−7.54	0.92
85	24.78	0.56	9.15	0.70	10.74	0.74
50	−5.69	0.85	−11.17	0.64	−8.21	0.90
52	−3.00	0.89	−9.86	0.57	−5.86	0.82
55	2.99	0.26	2.74	0.11	2.80	0.33
166	20.03	0.85	−5.90	0.83	−21.41	0.82
183 ± 1	3.67	0.68	1.13	0.69	−1.11	0.66
183 ± 3	8.01	0.83	−5.40	0.89	−14.33	0.88
183 ± 7	16.92	0.86	−5.23	0.88	−20.32	0.87
183 ± 10	20.73	0.87	−3.62	0.87	−19.91	0.84

[51] **Acknowledgments.** We wish to thank the Global Hydrology Center at NASA Marshall Space Flight Center for providing the instrument data at a unified webpage. We also thank the instrument Principal Investigators Jeff Halverson for the dropsonde data, Gerald Heymsfield for the EDOP data, Robbie Hood for the AMPR data, and Bjorn Lambrigtsen for the HAMSR data. We wish to thank Scott Braun and Liguang Wu for the MM5 simulated data. We thank Ben Johnson and Faith Collins for helpful discussions and studies that supported this work. The helpful comments of our three anonymous reviewers added to the clarity and robustness of this work. We acknowledge the Missouri Space Consortium and NASA Goddard for summer student support of Eric Holthaus and Cerese Albers. Interest in our work by Dr. Ramesh Kakar of Code Y at NASA HQ is also gratefully appreciated.

References

Auer, A. H., and D. L. Veal (1970), The dimension of ice crystals in natural clouds, *J. Amos. Sci.*, *27*, 919–926.

Bennartz, R., and P. Bauer (2003), Sensitivity of microwave radiances at 85–183 GHz to precipitating ice particles, *Radio Sci.*, *38*(4), 8075, doi:10.1029/2002RS002626.

Black, R. A., and J. Hallett (1986), Observations of the distributions of ice in hurricanes, *J. Atmos. Sci.*, *43*, 802–822.

Bohren, C. F., and L. J. Battan (1980), Radar backscattering by inhomogeneous precipitating particles, *J. Atm. Sci.*, *37*, 1821–1827.

Brown, P. R., and P. N. Francis (1995), Improved measurements of the ice water content in cirrus using a total-water probe, *J. Atmos. Oceanic Technol.*, *12*, 410–414.

Draine, B. T., and P. J. Flatau (1994), Discrete dipole approximation for scattering calculations, *J. Opt. Soc. Am.*, *A11*, 1491–1499.

Gasiewski, A. J. (1993), Microwave radiative transfer in hydrometeors, in *Atmospheric Remote Sensing by Microwave Radiometry*, edited by M. A. Janssen, pp. 91–144, John Wiley and Sons.

Halverson, J. B., J. Simpson, G. Heymsfield, H. Pierce, T. Hock, and L. Ritchie (2006), Warm core structure of Hurricane Erin diagnosed from high altitude dropsondes during CAMEX-4, *J. Atmos. Sci.*, *63*, 309–324.

Heymsfield, G. M., S. Bidwell, I. J. Caylor, S. Ameen, S. Nicholson, W. Boncyk, L. Miller, D. Vandemark, P. E. Racette, and L. R. Dod (1996), The EDOP radar system on the high-altitude NASA ER-2 aircraft, *J. Atmos. Ocean. Technol.*, *13*, 795–809.

Heymsfield, A. J., A. Bansemer, S. L. Durden, R. L. Herman, and T. P. Bui (2006), Ice microphysics observations in Hurricane Humberto: Comparison with non-hurricane generated ice cloud layers, *J. Atmos. Sci.*, *63*, 288–308.

Heymsfield, A. J., et al. (2007), Testing IWC retrieval methods using radar and ancillary measurements with in situ data, *J. Appl. Meteor. Cli.*, Accepted June 2007.

Hitschfeld, W., and J. Bordan (1954), Errors inherent in the radar measurement of rainfall at attenuating wavelengths, *J. Meteorol.*, *11*, 58–67.

Jensen, E., D. Starr, and O. B. Toon (2004), Mission investigates tropical cirrus clouds, *EOS*, *85*, 45–50.

Kakar, R., M. Goodman, R. Hood, and A. Guillory (2006), Overview of the Convection and Moisture Experiment (CAMEX), *J. Atmos. Sci.*, *63*, 5–18.

Kim, M.-J. (2006), Single scattering parameters of randomly oriented snow particles at microwave frequencies, *J. Geophys. Res.*, *111*, D14201, doi:10.1029/2005JD006892.

Kim, M.-J., G. M. Skofronick-Jackson, and J. A. Weinman (2004), Intercomparison of millimeter-wave radiative transfer models, *IEEE Trans. Geosci. Remote Sens.*, *42*, 1882–1890.

Kim, M.-J., J. A. Weinman, W. S. Olson, D.-E. Chang, G. Skofronick-Jackson, and J. R. Wang (2007), A Physical Model to Estimate Snowfall over Land using AMSU-B Observations, Accepted *J. Geophys. Research*, July 2007.

Lambrigtsen, B. H., and A. L. Riley (2002), Microwave Scattering Observed in Convective Cells During CAMEX-4. Proceedings AMS 25th Conference on Hurricanes and Tropical Meteorology; San Diego, CA, 13A.6.

Liu, G. (2004), Approximation of single scattering properties of ice and snow particles for high microwave frequencies, *J. Atmos. Sci.*, *61*, 2441–2456.

Marshall, J. S., and W. M. Palmer (1948), The distribution of raindrops with size, *J. Meteorol.*, *5*, 165–166.

McFarquhar, G. M., H. Zhang, G. Heymsfield, R. Hood, J. Dudhia, J. B. Halverson, and F. Marks Jr. (2006), Factors affecting the evolution of Hurricane Erin and the distributions of hydrometeors: Role of microphysical processes, *J. Atmos. Sci.*, *63*, 127–150.

Monahan, E. C., and D. K. Woolf (1989), "Comments on "variations of whitecap coverage with wind stress and water temperature", *J. Phys. Oceanogr.*, *19*, 706–709.

Olson, W. S., P. Bauer, N. F. Viltard, D. E. Johnson, W. K. Tao, R. Meneghini, and L. Liao (2001), A melting-layer model for passive/active microwave remote sensing applications. Part I: Model formulation and comparison with observations, *J. Appl. Meteorol.*, *40*, 1145–1163.

Skofronick-Jackson, G. M., A. J. Gasiewski, and J. R. Wang (2002), Influence of microphysical cloud parameterizations on microwave brightness temperatures", *IEEE Trans. Geosci. Remote Sens.*, *40*, 187–196.

Skofronick-Jackson, G. M., J. R. Wang, G. M. Heymsfield, R. Hood, W. Manning, R. Meneghini, and J. A. Weinman (2003), Combined radiometer-radar microphysical profile estimations with emphasis on high frequency brightness temperature observations", *J. of Appl. Meteorol.*, *42*, 476–487.

Skofronick-Jackson, G. M., M. J. Kim, J. A. Weinman, and D. E. Chang (2004), A physical model to determine snowfall over land by microwave radiometry, *IEEE Trans. Geosci. Remote Sens.*, *42*, 1047–1058.

Spencer, R. W., R. E. Hood, F. J. LaFontaine, E. A. Smith, R. Platt, J. Galliano, V. L. Griffin, and E. Lobl (1994), High-resolution imaging of rain systems with the advanced microwave precipitation radiometer, *J. Atmos. Ocean. Technol.*, *11*, 849–857.

Tao, W.-K., and J. Simpson (1993), Goddard cumulus ensemble model. Part I: Model description, *Terr. Atmos. Oceanic Sci.*, *4*, 35–72.

Tao, W.-K., J. Shi, S. Chen, S. Lang, S.-Y. Hong, C. Peters-Lidard, S. Braun, and J. Simpson (2007), Revised bulk-microphysical schemes for studying precipitation processes. Part I: Comparisons with other schemes, Submitted to *Mon. Wea. Rev.* February 2007.

Willoughby, H. E. (1998), Tropical cyclone eye thermodynamics, *Mon. Weather Rev.*, *126*, 3053–3067.

Willoughby, H., D. Jorgensen, R. Black, and S. Rosenthal (1985), Project STORMFURY: A scientific chronicle 1962–1983, *Bull. Am. Meteorol. Soc.*, *66*, 505–514.

Wu, L., S. A. Braun, J. Halverson, and G. Heymsfield (2006), A numerical study of Hurricane Erin (2001). Part I: Model verification and storm evolution, *J. Atmos. Sci.*, *63*, 65–86.

Xu, Y.-L., and B. A. S. Gustafson (2001), A generalized multiparticle mie-solution: Further experimental verification, *JQSRT*, *70*, 395–419.

C. Albers, Florida State University, Tallahassee, FL, USA.

A. Heymsfield, National Center for Atmospheric Research, Boulder, CO, USA.

E. Holthaus, Columbia University, New York City, NY, USA.

M.-J. Kim, NOAA, Camp Springs, MD, USA.

G. Skofronick-Jackson, NASA Goddard Space Flight Center, Code 614.6, Building 33, Room A428, Greenbelt, MD 20771, USA. (gail.s.jackson@nasa.gov)